

# Optics Letters

## Plasmon modes of a silver thin film taper probed with STEM-EELS

FRANZ-PHILIPP SCHMIDT,<sup>1,2,\*</sup> HARALD DITLBACHER,<sup>2</sup> ANDREAS TRÜGLER,<sup>2</sup> ULRICH HOHENESTER,<sup>2</sup> ANDREAS HOHENAU,<sup>2</sup> FERDINAND HOFER,<sup>1</sup> AND JOACHIM R. KRENN<sup>2</sup>

<sup>1</sup>Institute for Electron Microscopy and Nanoanalysis (FELMI), Graz University of Technology, Steyrergasse 17, 8010 Graz, Austria

<sup>2</sup>Institute of Physics, Karl-Franzens-University, Universitätsplatz 5, 8010 Graz, Austria

\*Corresponding author: franz.schmidt@felmi-zfe.at

Received 21 October 2015; revised 5 November 2015; accepted 7 November 2015; posted 9 November 2015 (Doc. ID 252090); published 26 November 2015

**By focusing propagating surface plasmons, electromagnetic energy can be delivered to nanoscale volumes. In this context, we employ electron energy loss spectroscopy in a scanning transmission electron microscope to characterize the full plasmonic mode spectrum of a silver thin film tapered to a sharp tip. We show that the plasmon modes can be ordered in film and edge modes and corroborate our assignment through supplementary numerical simulations. In particular, we find that the focused plasmon field at the taper tip is fueled by edge modes.** © 2015 Optical Society of America

**OCIS codes:** (250.5403) Plasmonics; (240.6680) Surface plasmons; (310.6628) Subwavelength structures, nanostructures; (220.4241) Nanostructure fabrication.

<http://dx.doi.org/10.1364/OL.40.005670>

Plasmonic nanostructures enable the concentration of light to the deep subwavelength regime and, thus, are the topic of intense fundamental and application oriented research [1]. Nanoparticles acting as optical antennas are well known for their nanoscale mode volumes, due to the excitation of localized plasmon modes [2]. In contrast, tapered metal waveguides can concentrate propagating plasmon waves as the plasmon waveguide cross section decreases [3,4]. In particular, in the case of adiabatic tapering, a strong focusing effect that is limited by the metal skin depth only is to be expected [5]. Plasmon concentration on 3D conical tapers, i.e., sharpened metal tips, has been experimentally realized [6] and has found applications in scanning probe based spectroscopy [7,8]. Besides the conical taper, 3D wedge tapers [9] and 2D (thin film) tapers [10,11] were applied for plasmon nanofocusing. The 2D variant is of particular interest, as it provides compatibility with thin film technology, including relative ease of fabrication. In this Letter, we probe the plasmonic mode spectrum of a sharply tapered silver thin film with high spatial resolution by means of electron energy loss spectroscopy (EELS) in a scanning transmission electron microscope (STEM). We identify a rich mode

spectrum and show that it can be decomposed into film and edge plasmon modes, in accordance with numerical simulations. In particular, we show that the enhanced focused plasmon field at the taper tip is fueled by edge modes.

A laterally tapered 30 nm thick silver film on a 30 nm thick Si<sub>3</sub>N<sub>4</sub> substrate was fabricated by electron beam lithography with a standard silver evaporation and lift-off procedure [12]. The choice of the silver thickness was motivated by minimizing electron transmission loss, preventing multiple electron scattering and impeding significant coupling of plasmon modes on the top and bottom film interfaces. The taper has a length of 5 μm, an opening angle of 11.4°, and a tip radius of about 50 nm. Due to the presence of the substrate, symmetric and antisymmetric (with respect to the magnetic field component) plasmon modes exist, with field maxima at the silver/air and silver/Si<sub>3</sub>N<sub>4</sub> interfaces, respectively. Accordingly, symmetric and antisymmetric modes exist for the edge plasmons [13]. Here, we concentrate on the antisymmetric modes which are truly bound excitations in contrast to the symmetric mode type [10,13].

Measuring the energy loss of an electron beam passing by or penetrating through a nanostructure provides a means of probing the local density of states LDOS (projected in the direction of the electron trajectory) of the optical mode spectrum [14,15]. STEM-EELS systems can provide a spatial resolution in the nm range and a spectral resolution of the order of 100 meV (recent developments enabling 10 meV [16]) and, thus, are well suited for the detailed probing of plasmon modes [17–19]. For our experiments, we used an FEI Tecnai F20 STEM with a monochromated 200 keV electron beam with an energy width of 300 meV (full width at half-maximum). Electron energy loss (EEL) spectra were acquired with a high-resolution Gatan imaging filter and a charge-coupled device camera with 2048 × 2048 pixels and an energy dispersion of 0.01 eV/channel. Electrons up to a semi-angle of 2.2 mrad were collected, and the exposure time per EEL spectrum was 0.2 s. The spectra were acquired from scan areas of 2885 nm × 869 nm, with a scan step size of about 35 nm. EEL data were deconvolved using the Richardson–Lucy algorithm (MathWorks Matlab, deconvlucy function), implemented in

a homemade analysis program (“SI analysis tool—A flexible MATLAB tool to analyze spectrum images” available at <http://esteem2.eu> in the section “Software”), except in Figs. 1(a) and 1(b), where the raw data are shown. Energy-resolved maps (EEL maps) of the scan region were extracted from the measured data set by applying an energy window of 0.2 eV around the loss energy of interest. In addition, EEL maps integrated over the full spectral range are used for sample overview. STEM images were acquired with a high-angle annular dark field (HAADF) detector (Fischione Instruments) under a convergence semi-angle of 7.3 mrad.

Starting with the film surface of the taper, EEL spectra acquired within areas along the taper symmetry axis (as marked in the EEL map integrated over the full spectral range in the inset) are plotted in Fig. 1(a). The prominent peak labeled  $F_A^2$  (corresponding to a second-order standing plasmon wave, as shown below) shifts to higher energies as the taper tip is approached. Probing the areas off the taper axis [as marked in the inset in Fig. 1(b)] strongly modifies the spectral signature showing again, however, a shifting peak, labeled  $F_A^3$  [corresponding

to a third-order standing plasmon wave, Fig. 1(b)]. For closer investigation, we deconvolve the EEL spectra and compare the data acquired in areas I and II at taper widths of  $300 \pm 10$  nm and  $450 \pm 10$  nm, respectively, as indicated in the HAADF image and the EEL map in Fig. 1(c). In area I, peak  $F_A^2$  appears at 2.24 eV and shifts to 1.88 eV in area II. Conversely, peak  $F_A^3$  shifts from 2.57 eV in I to 2.24 eV in II. As we will further substantiate with EEL maps below, we interpret this as signatures for the standing modes of second and third-order of the antisymmetric (A) film plasmon in the vertical direction of the taper, in analogy to former observations on silver disks [20]. The concurrent observation of the loss energy peak at 2.24 eV (corresponding to a free space wavelength of 554 nm) for taper widths of 300 and 450 nm implies a half-plasmon mode wavelength close to 150 nm, i.e., a plasmon wavelength of 300 nm. For this energy, this corresponds to an effective mode index of  $n_{\text{eff}} = 1.85$ . Considering the rather small thickness of the  $\text{Si}_3\text{N}_4$  substrate (refractive index 2.0 for a wavelength of 554 nm) of 30 nm (i.e., of the order of the plasmon field extension), this is a plausible result and in accordance with even smaller values found for 15 nm thick substrates [13]. We note that considering a phase shift upon plasmon reflection (as briefly discussed below) does not change our mode assignment which is set by the observed plasmon wavelength of 300 nm.

The film plasmon modes are imaged in the EEL maps in Fig. 2(a) for loss energies between 1.47 and 2.78 eV. With increasing energy, we observe the emergence of a horizontally aligned loss feature (marked by the white arrow) that splits into two features for higher energies (black arrows). These features shift to smaller taper widths with increasing loss energy (corresponding to smaller wavelength), in accordance with the peak energies in Fig. 1(a). This substantiates our interpretation of the film plasmon forming standing waves due to reflection at the taper edges, corresponding to the  $F_A^2$  and  $F_A^3$  modes defined above. The mode patterns become even clearer in the cross sections in Fig. 2(b), averaged over the boxes in the EEL maps for 1.47 and 2.05 eV, showing  $F_A^2$  and  $F_A^3$ , respectively. For the highest energy values, the pattern visibility in the EEL maps is lost, most probably due to increased loss.

We corroborate our experimental results with numerical simulations based on the MNPBEM toolbox [21] that relies on the boundary element method, and its EELS extension [22]. A simulated EEL map at 2.24 eV is shown in Fig. 2(c), calculated for a taper geometry corresponding to the sample and the dielectric function of silver taken from [23]. The substrate was not taken into account, and the surrounding medium was assigned a refractive index of 1. Apart from a resulting shift of mode frequencies that leads us to compare the experimental EEL map at 2.05 eV with the simulation, we find that the simulated film mode pattern corresponds very well to the observations, evidencing our interpretation of standing film plasmon modes [Fig. 2(c)]. In addition, the simulation confirms the striking absence of the first-order  $F_A^1$  mode from the film plasmon pattern, most probably due to increased loss at the higher energies corresponding to the small wavelength necessary to fulfill the  $F_A^1$  resonance condition.

As mentioned before, a phase shift  $\phi$  upon plasmon reflection from the edges can modify the resonance taper width  $d$  for the  $m$ th mode order, according to  $kd + \phi = m\pi$  ( $k$  plasmon wave number). We find from the spectral data in Figs. 1 and 2 that the phase shift is close to zero. It should be noted that work

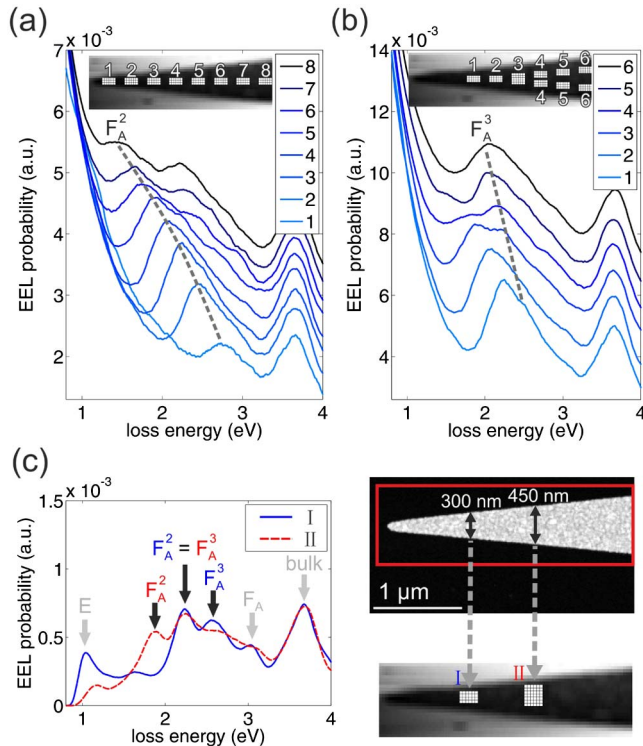


**Fig. 1.** Position dependent EEL spectra. (a) EEL spectra acquired at the positions along the taper symmetry axis as indicated in the EEL maps integrated over the full spectral range in the inset. The dashed line follows the position-dependent spectral evolution of the  $F_A^2$  mode. (b) EEL spectra acquired at the positions as marked in the inset; spectra from regions with the same number are summed up. The dashed line follows the position-dependent spectral evolution of the  $F_A^3$  mode. The original spectra were smoothed by nearest-neighbor averaging, normalized to their zero-loss peak maxima and offset for clarity of presentation. (c) Deconvolved EEL spectra acquired within areas I and II as marked in the HAADF image and EEL map. Further peaks in the spectrum can be assigned to the edge modes (E) discussed below, the asymptotic part of the antisymmetric film plasmon ( $F_A$ ) [13], and the bulk plasmon of silver.

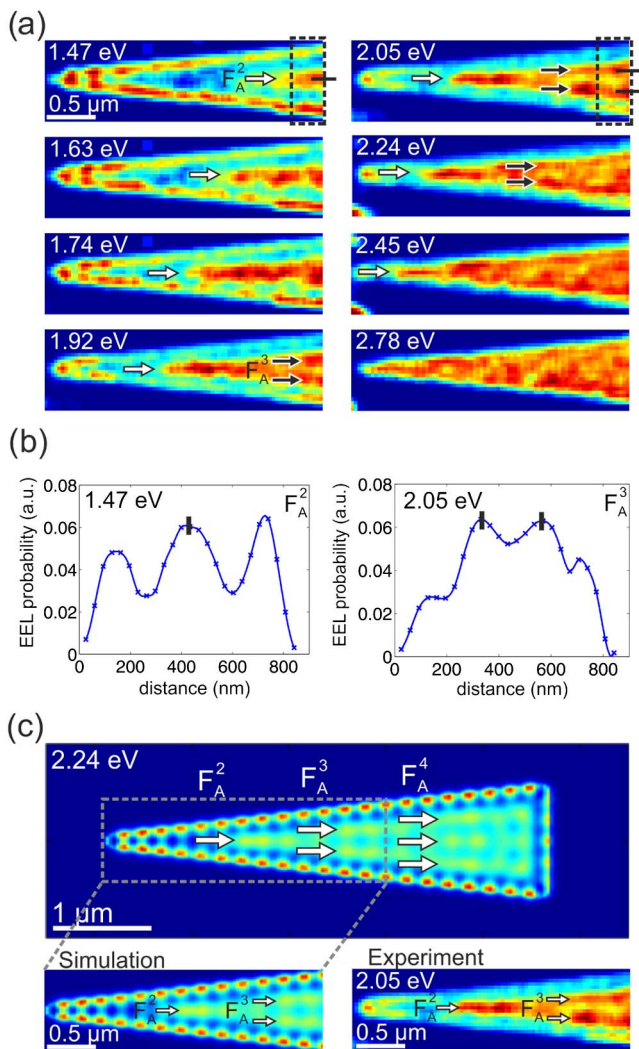


**Fig. 2.** Spectrally resolved EEL maps. (a) Experimental EEL maps at energies between 1.47 to 2.78 eV showing the spatial evolution of the  $F_A^2$  and  $F_A^3$  modes. The color range has been individually adapted to the maximum signal range in each map. (b) Cross-cuts in vertical directions from the EEL maps at 1.47 and 2.05 eV, averaged over the boxes in the corresponding EEL maps. (c) Simulated EEL map at 2.24 eV of a silver taper with the same dimensions as in the experiment. The arrows depict the second-, third- and fourth-order film modes in vertical directions (top). A magnified view on the simulated EEL-map and the corresponding experimental EEL map (bottom) at a loss energy of 2.05 eV.

on similar plasmonic geometries has reported significant phase shifts [11,24]. This could be due to the specific taper geometry or the used substrate, a clear assignment requiring additional studies.

We now turn to lower loss energy values, plotting in Fig. 3(a) deconvolved EEL spectra in the energy range 0.8–1.8 eV, as acquired at the positions 1–4 marked in the inset. EEL maps for the corresponding peak energies A–D are shown in Fig. 3(b). It is evident from these maps that we are dealing with edge modes here. As less charge is involved at the edges (compared to the film surface), the edge plasmons appear at lower energies [13]. From the EEL maps, two prominent features become evident. First, a strongly localized intensity

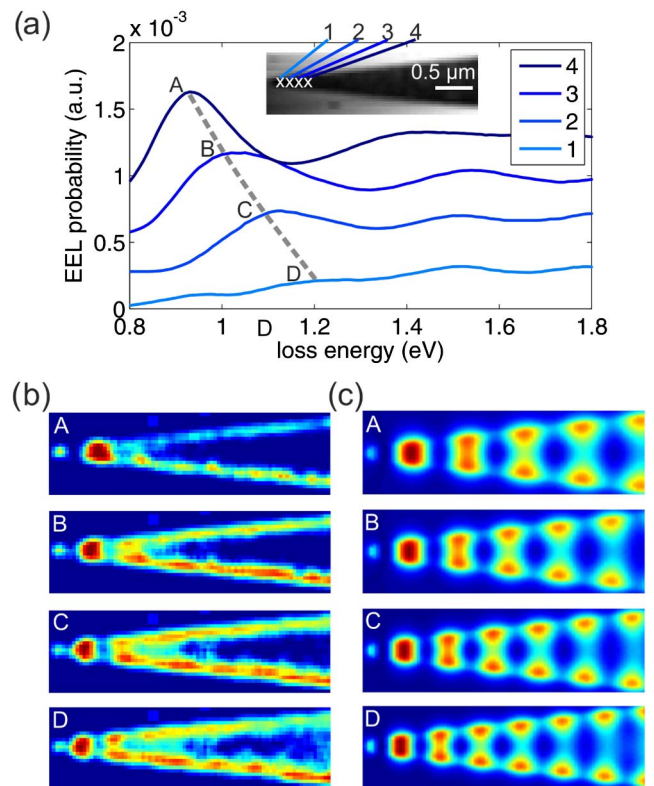


**Fig. 3.** (a) Experimental EEL spectra close to the tip region of the silver taper. (b) Experimental and (c) simulated EEL maps of the silver taper at the energy loss corresponding to the peak energies as indicated in (a): A 0.93 eV, B 1.03 eV, C 1.13 eV, and D 1.24 eV.

maximum at the very tip of the taper that can be assigned to field enhancement due to the geometric tip effect. Second, a much stronger feature occurs at an energy-dependent distance from the tip. It seems evident that this feature is due to constructive interference of the edge modes that are thus leading to plasmon field confinement in the 2D taper geometry, in contrast to the film modes (Fig. 2). The intensity ratio of this “hot spot” relative to the spot at the taper tip is expected to be determined by the chosen taper geometry in a balance between plasmon localization and loss, and could thus probably be tuned by optimizing the taper geometry. In addition, an according optical excitation of the edges can be envisaged to include active control of the “hot spot” by introducing a phase shift between both edge modes. In the simulations in Figs. 2 and 3, we observe a periodic modulation of the edge mode that is due to interference of edge plasmons reflected from the front and back taper tips. This feature cannot be observed in the experiment due to a spectral resolution (300 meV) that is too small to resolve the free spectral range of about 120 meV of the edge modes. In addition, a higher damping and a lower reflection value of the edge modes (due to, e.g., surface roughness) in the experiment might be of importance. Further simulations over the full spectral range for an effective mode index of  $n_{\text{eff}} = 1.85$ , in particular highlighting the origin of the edge mode modulation in plasmon reflection are summarized in a Visualization 1 in the Appendix A.

In summary, we have ordered the full mode spectrum of a 2D silver taper as retrieved by STEM-EELS into film and edge

modes. The film modes form standing wave patterns, while the edge modes fuel the plasmon field concentration close to the taper tip. Finally, it is interesting to note that we observe a striking similarity to the plasmon patterns observed on a tapered graphene layer of similar geometry [25,26].

## APPENDIX A

The *Visualization 1* shows two EEL map movies simulated by the Matlab toolbox MNPBEM (as described in the main text) for the energies marked in the EEL spectrum in the top panel. The simulations were done for the parameters used in Figs. 2 and 3 of the main text, except a medium refractive index of 1.85. While this choice corresponds to the measured effective index of the film plasmon at an energy of 2.24 eV, here it should be understood rather as a value illustrating the impact of a higher index medium than a full model of the experimental system, as the dispersion-induced energy dependence of the effective index is not taken into account.

The EEL spectrum was calculated at the taper tip as sketched in the inset of the top panel. It shows a series of peaks that reflect the occurrence of edge mode resonances, following our findings in the main text. The EEL maps in the middle and bottom panels are calculated for peak (blue lines) and valley energies (red lines), respectively. We find a marked modulation of the plasmon energy along the edges for the peak positions due to standing edge waves. Either no modulation or a much weaker contrast is observed for the valley energy positions. On the other hand, no significant dependence of the film modes on the choice of peak or valley energies is observed.

**Funding.** European Union Seventh Framework Programme (ESTEEM2) (312483); FWF SFB NextLite (F4905-N23, F4906-N23, P27299-N27); NAWI Graz and the Graz Center for Electron Microscopy (ZFE Graz).

## REFERENCES

1. S. A. Maier, *Plasmonics: Fundamentals and Applications: Fundamentals and Applications* (Springer, 2007).
2. P. Bharadwaj, B. Deutsch, and L. Novotny, *Adv. Opt. Photonics* **1**, 438 (2009).
3. A. J. Babadjanyan, N. L. Margaryan, and K. V. Nerkararyan, *J. Appl. Phys.* **87**, 3785 (2000).
4. D. K. Gramotnev and S. I. Bozhevolnyi, *Nat. Photonics* **8**, 14 (2014).
5. M. I. Stockman, *Phys. Rev. Lett.* **93**, 137404 (2004).
6. B. Schröder, T. Weber, S. V. Yalunin, T. Kiel, C. Matyssek, M. Sivilis, S. Schäfer, F. V. Cube, S. Irsen, K. Busch, C. Ropers, and S. Linden, *Phys. Rev. B* **92**, 085411 (2015).
7. S. Berweger, J. M. Atkin, R. L. Olmon, and M. B. Raschke, *J. Phys. Chem. Lett.* **1**, 3427 (2010).
8. F. D. Angelis, G. Das, P. Candeloro, M. Patrini, M. Galli, A. Bek, M. Lazzarino, I. Maksymov, C. Liberale, L. C. Andreani, and E. Di Fabrizio, *Nat. Nanotechnol.* **5**, 67 (2010).
9. K. C. Vernon, D. K. Gramotnev, and D. F. P. Pile, *J. Appl. Phys.* **101**, 104312 (2007).
10. E. Verhagen, A. Polman, and L. Kuipers, *Opt. Express* **16**, 45 (2008).
11. E. S. Barnard, T. Coenen, E. J. R. Vesseur, A. Polman, and M. L. Brongersma, *Nano Lett.* **11**, 4265 (2011).
12. A. Hohenau, H. Ditlbacher, B. Lamprecht, J. R. Krenn, and F. R. Aussenegg, *Microelectron. Eng.* **83**, 1464 (2006).
13. F.-P. Schmidt, H. Ditlbacher, U. Hohenester, A. Hohenau, F. Hofer, and J. R. Krenn, *Nat. Commun.* **5**, 3604 (2014).
14. F. J. García de Abajo and M. Kociak, *Phys. Rev. Lett.* **100**, 106804 (2008).
15. U. Hohenester, H. Ditlbacher, and J. R. Krenn, *Phys. Rev. Lett.* **103**, 106801 (2009).
16. O. L. Krivanek, T. C. Lovejoy, N. Dellby, T. Aoki, R. W. Carpenter, P. Rez, E. Soignard, J. Zhu, P. E. Batson, M. J. Lagos, R. F. Egerton, and P. A. Crozier, *Nature* **514**, 209 (2014).
17. J. Nelayah, M. Kociak, O. Stephan, J. F. Garcia de Abajo, M. Tence, L. Henrard, D. Taverna, I. Pastoriza-Santos, L. M. Liz-Marzan, and C. Colliex, *Nat. Phys.* **3**, 348 (2007).
18. B. Schaffer, U. Hohenester, A. Trügler, and F. Hofer, *Phys. Rev. B* **79**, 041401(R) (2009).
19. O. Nicoletti, F. de la Peña, R. K. Leary, D. J. Holland, C. Ducati, and P. A. Midgley, *Nature* **502**, 80 (2013).
20. F.-P. Schmidt, H. Ditlbacher, U. Hohenester, A. Hohenau, F. Hofer, and J. R. Krenn, *Nano Lett.* **12**, 5780 (2012).
21. U. Hohenester and A. Trügler, *Comput. Phys. Commun.* **183**, 370 (2012).
22. U. Hohenester, *Comput. Phys. Commun.* **185**, 1177 (2014).
23. P. B. Johnson and R. W. Christy, *Phys. Rev. B* **6**, 4370 (1972).
24. T. Søndergaard, J. Beermann, A. Boltasseva, and S. I. Bozhevolnyi, *Phys. Rev. B* **77**, 115420 (2008).
25. J. Chen, M. Badioli, P. Alonso-Gonzalez, S. Thongrattanasiri, F. Huth, J. Osmond, M. Spasenovic, A. Centeno, A. Pesquera, P. Godignon, A. Zurutuza Elorza, N. Camara, J. F. Garcia de Abajo, R. Hillenbrand, and F. H. L. Koppens, *Nature* **487**, 77 (2012).
26. Z. Fei, A. S. Rodin, G. O. Andreev, W. Bao, A. S. McLeod, M. Wagner, L. M. Zhang, Z. Zhao, M. Thieme, G. Dominguez, M. M. Fogler, A. H. Castro Neto, C. N. Lau, F. Keilmann, and D. N. Basov, *Nature* **487**, 82 (2012).